High performance filtering and high-sensitivity concentration retrieval of methane in photoacoustic spectroscopy utilizing deep learning residual networks

Yanan Cao [a,b,c], Yan Li [a,c], Wenlei Fu [a,c], Gang Cheng [a,c,*], Xing Tian [a,c], Jingjing Wang [d,**], Shenlong Zha [e], Junru Wang [f]

[a] *The First Hospital of Anhui University of Science and Technology, Huainan 232001, China*
[b] *Anhui Zhongzhi Rail Transit Equipment Manufacturing Co., Ltd, Huainan 232001, China*
[c] *State Key Laboratory of Mining Response and Disaster Prevention and Control in Deep Coal Mines, Anhui University of Science and Technology, Huainan 232001, China*
[d] *Department of Atmospheric and Oceanic Sciences, Fudan University, Shanghai 200433, China*
[e] *School of Electronic Engineering and Intelligent Manufacturing, Anqing Normal University, Anqing 246000, China*
[f] *College of Electronic Engineering, National University of Defense Technology, Hefei 230037, China*

ARTICLE INFO

ABSTRACT

A novel method is introduced to improve the detection performance of photoacoustic spectroscopy for trace gas detection. For effectively suppressing various types of noise, this method integrates photoacoustic spectroscopy with residual networks model which encompasses a total of 40 weighted layers. Firstly, this approach was employed to accurately retrieve methane concentrations at various levels. Secondly, the analysis of the signal-to-noise ratio (SNR) of multiple sets of photoacoustic spectroscopy signals revealed significant enhancement. The SNR was improved from 21 to 805, 52–962, 98–944, 188–933, 310–941, and 587–936 across the different concentrations, respectively, as a result of the application of the residual networks. Finally, further exploration for the measurement precision and stability of photoacoustic spectroscopy system utilizing residual networks was carried out. The measurement precision of 0.0626 ppm was obtained and the minimum detectable limit was found to be 1.47 ppb. Compared to traditional photoacoustic spectroscopy method, an approximately 46-fold improvement in detection limit and 69-fold enhancement in measurement precision were achieved, respectively. This method not only advances the measurement precision and stability of trace gas detection but also highlights the potential of deep learning algorithms in spectroscopy detection.

1. Introduction

The precise quantitative detection of trace gases is receiving an increasing attention in various industry fields such as industrial process control, pollution environmental monitoring, combustion characterization, earth observation systems, medical diagnosis, and food safety [1–3]. Compared with cavity-enhanced absorption spectroscopy (CEAS) [4,5], cavity ring-down spectroscopy (CRDS)[6–12], Fourier transform infrared spectroscopy(FTIR) [13,14], tunable diode laser absorption spectroscopy (TDLAS)[15,16], quartz-enhanced photoacoustic spectroscopy (QEPAS)[17–23], light-induced thermoelastic spectroscopy

(LITES)[24–26], frequency comb spectroscopy(FCS) [27–30], etc., the photoacoustic spectroscopy (PAS) has been developed rapidly and widely used for the analysis of trace gases, owing to its high sensitivity, fast response, high selectivity, non-contact real-time continuous measurement, multi-component detection, etc. [31–36]. However, the performance of the PAS is affected by intrinsic noises induced by electrical components. As a variant of wavelength modulation spectroscopy (WMS), the PAS only focuses on reducing low-frequency noise ($1/f$ noise) to improve detection sensitivity, which isn't efficient for other noise types(optical interference fringe noise). Therefore, it is of great significance to effectively extract the weak photoelectric absorption
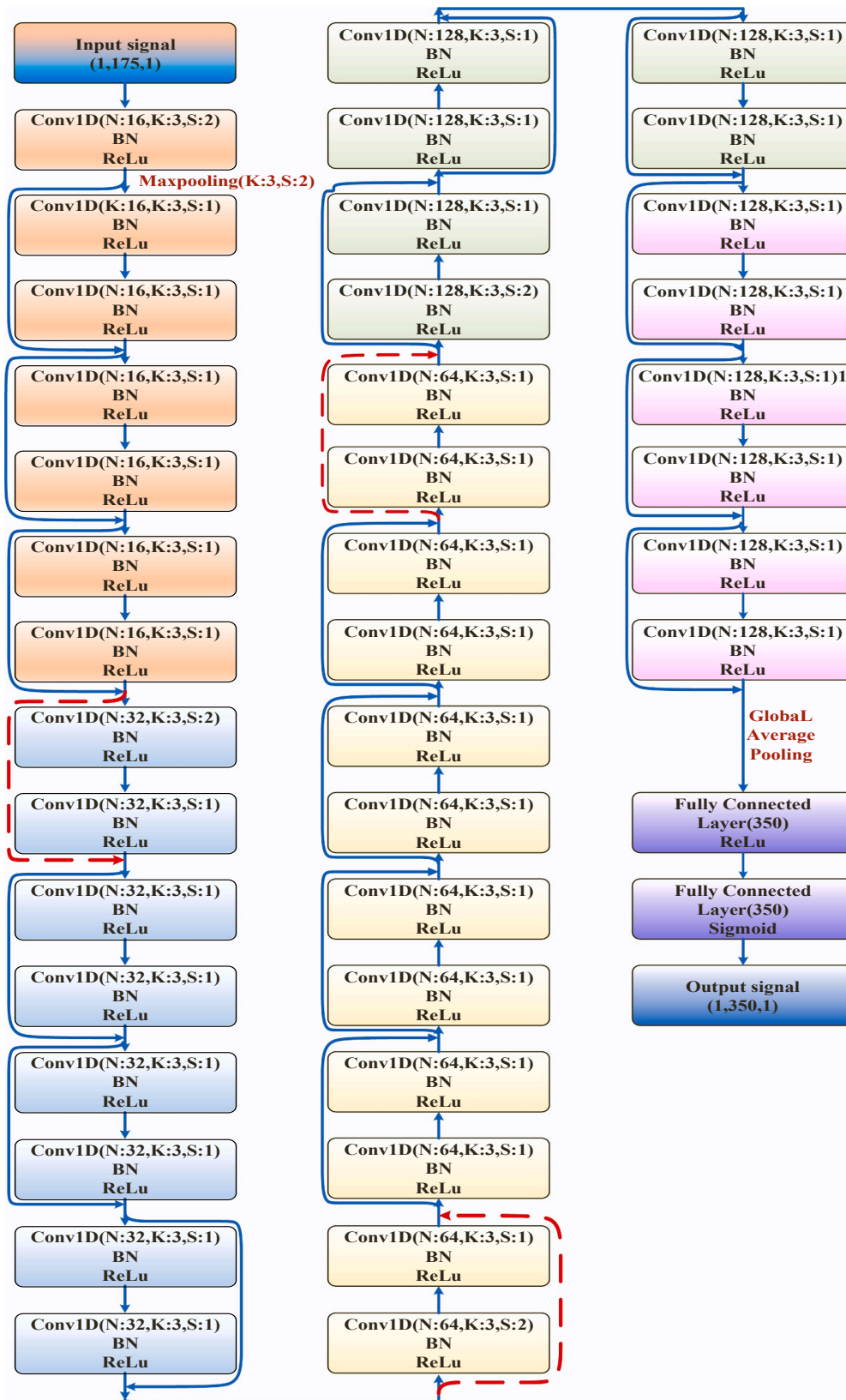
Fig. 1. Network architectures for ResNets. Abbreviation: N: Number of convolution kernels; K: Kernel size; S: Stride.

signals from strong background noise.

Several different methods have been proposed to eliminate the negative influence of the noise. The traditional methods for weak signal processing mainly encompass the multi-signal averaging filtering (MAF) method, electronic filter method, wavelet transform denoising method, correlation detection method and parameter-tuning stochastic resonance (SR) filtering method. ① The multi-signal averaging filtering (MAF) method is capable of yielding a signal with a high signal-to-noise
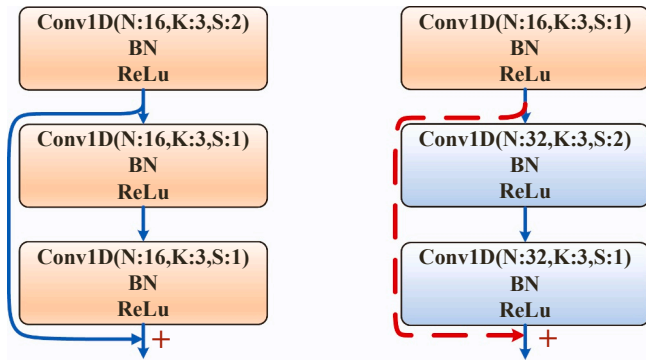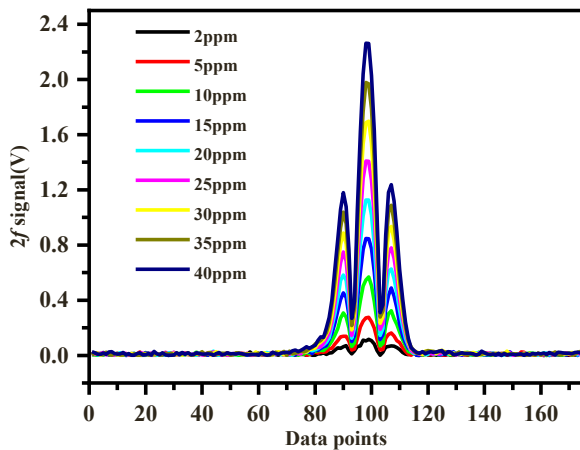
Fig. 2. Resnets: shortcut connections.

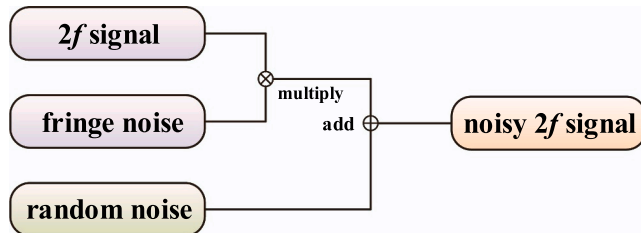**Fig. 3.** PAS 2f signals at different concentrations.

Fig. 4. Obtaining noisy signal diagram.

ratio (SNR). However, it is limited in its ability to suppress random noise, and it is so time-consuming that it is unsuitable for online signal processing. ②The electronic filters characterized by the narrow bandwidth are extensively employed for noise reduction. Nonetheless, when the bandwidths of noise and signal overlap, it is relatively arduous to design an electronic filter that precisely matches the signal's bandwidth to effectively eliminate the noise. ③The wavelet transform denoising method allows for efficient online filtering, However, when the useful signals and noise share overlapping bandwidths, its performance diminishes , as demonstrated by the suboptimal results. ④The correlation detection method is used to remove the noise by the autocorrelation of the periodic signal. At its core, it establishes a highly selective, narrow bandwidth filter to eliminate noise differing in frequency from the signal. ⑤The SR filtering method [37–39] possesses a unique advantage: even when the noise and signal's frequency band coincide, the SR method can transform a portion of the noise energy into signal energy, thereby suppressing noise and amplifying the useful signal. However, this method relies on intricate parameters and involves nonlinear

filtering processes.

To overcome the limitations inherent in the traditional filtering methods mentioned above, this study introduces a photoacoustic spectroscopy sensor system that leverages deep learning's residual networks (ResNets) for the precise measurement of methane (CH$_4$). In recent years, a variety of neural network architectures have emerged as tools for signal processing. Unlike Back Propagation (BP) neural networks, convolutional neural networks (CNNs), recurrent neural networks (RNNs), autoencoders, and generative adversarial networks (GANs) [40, 41], ResNets stand out due to their substantial network depth (ranging from tens to thousands of layers) and superior learning capability. This capability enhances the SNR without distorting the spectroscopy signal. in contrast to conventional MAF method, deep learning ResNets can process single signal in real-time online and achieve extremely high SNR; When juxtaposed with the electronic filters, correlation detection method, and SR filtering method, the ResNets can suppress and filter various types of noise such as random noise and periodic noise, while the ResNets is always in linear filtering mode. Unlike the wavelet transform denoising method, the pre-trained model of deep learning ResNets has excellent generalization ability and don't need to optimize the hyperparameters again.

2. Methods

2.1. Architecture of ResNets

In this paper, the ResNets based on one-dimensional convolutional neural networks are established. The specific architecture of the ResNets is illustrated in Fig. 1, which comprises 38 convolutional layer (Conv) modules, one max pooling layer, one global average pooling layer, and 2 fully connected layer modules. Based on the numbers of convolutional kernels and stride, each convolutional layer module conducts a convolution operation on the feature map. After convolution operation, the corresponding new feature maps are obtained. Next, a Batch Normalization (BN) operation is applied to bolster the model's generalization capability. After that, the ReLu activation function is performed to nonlinear transform the output feature map. The whole ResNets architecture executes a total of 38 convolution layers modules in sequence. Last, the network ends with a global average pooling layer, which is followed by two 350-way fully-connected layers. Two fully-connected layer modules utilize the ReLu and Sigmoid activation function to obtain the final retrieval outcome. The whole architecture encompasses a total of 40 weighted layers.

To enhance the network's depth and expressive capability, the shortcut connections are strategically integrated into the network, as depicted in Fig. 2.

The shortcut connections can be directly used to perform element-wise addition operation when the input and output are of the same dimensions (solid line shortcuts in Fig. 2). When the dimensions increase (red dotted line shortcuts in Fig. 2), a criterion can be followed: After extra zero entries padded for increasing dimensions, the shortcut connections still perform identity mapping. When the shortcut connections go across feature maps of two sizes, they are performed with a stride of 2.

2.2. Training and evaluation of ResNets

It is an extremely time-consuming and onerous task to obtain extensive datasets which is needed for training and testing ResNets model through PAS experiments. To address this issue, an innovative approach is adopted, the experiment initially yields a 148 ppm high-concentration methane PAS 2f signal, from which the background noise is meticulously subtracted to generate a pure methane PAS 2f signal with an impressive SNR of 587. In order to expedite the dataset creation process, this pure signal is then scaled to generate a vast array of methane PAS 2f signals across various concentrations at 2–40 ppm,
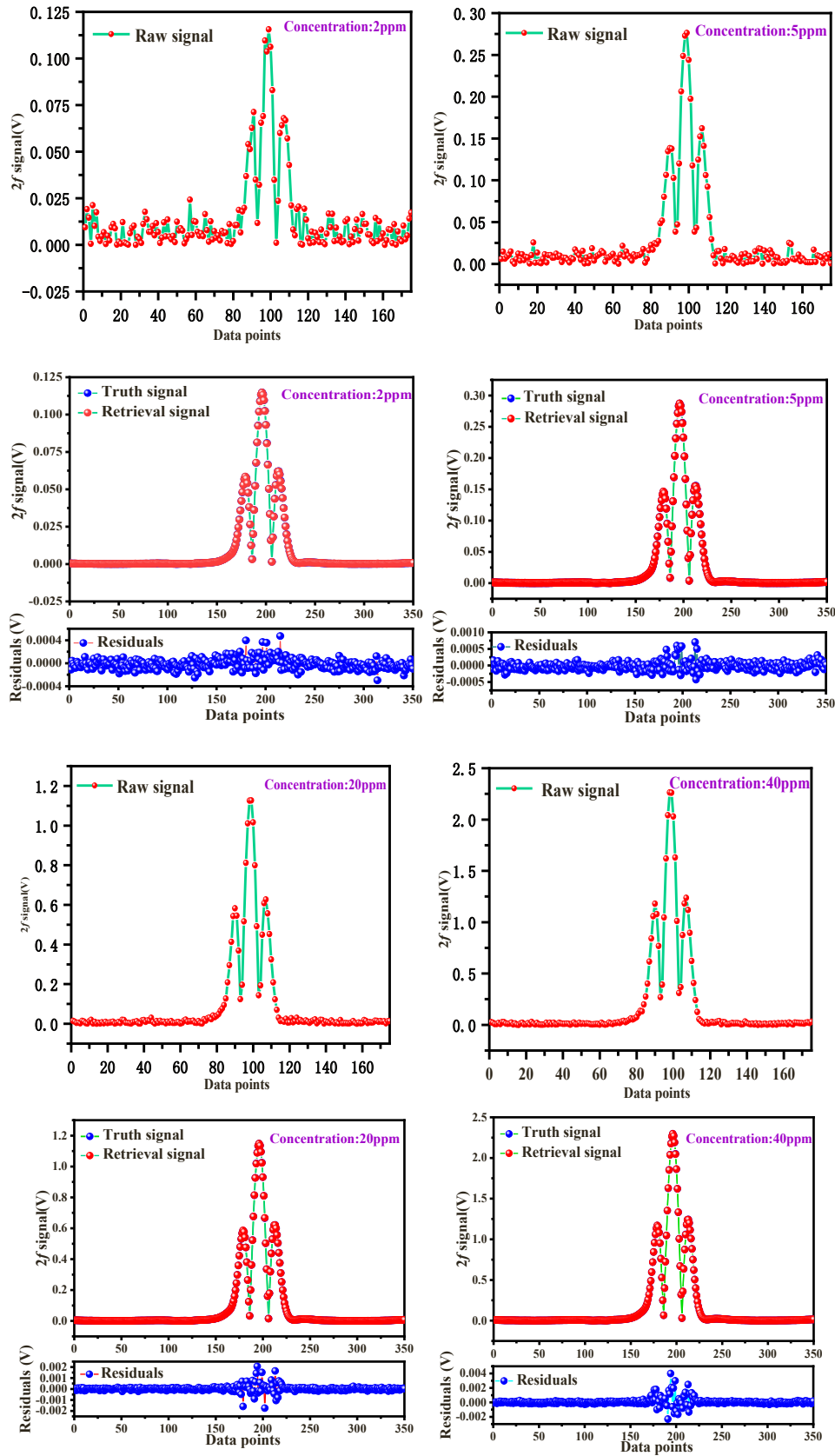
Fig. 5. Residual plots between truth signal and retrieval signal.

Table 1
Parameters of the PAS 2 *f* signal.

| Concentration	Input signal			Output signal		
	SD	Peak	SNR	SD	Peak	SNR
2 ppm	5.5*10–3	0.116	21	1.428*10–4	0.115	805
5 ppm	5.3*10–3	0.276	52	2.983*10–4	0.287	962
10 ppm	5.8*10–3	0.568	98	6.079*10–4	0.574	944
15 ppm	4.7*10–3	0.847	180	9.828*10–4	0.862	928
20 ppm	6.1*10–3	1.148	188	1.23*10–3	1.148	933
25 ppm	6.5*10–3	1.41	216	1.55*10–3	1.436	926
30 ppm	5.7*10–3	1.70	298	1.84*10–3	1.724	937
35 ppm	6.45*10–3	1.979	307	2.13*10–3	2.01	944
40 ppm	7.3*10–3	2.262	310	2.44*10–3	2.297	941
148 ppm	14.3*10–3	8.393	587	9.08*10–3	8.498	936
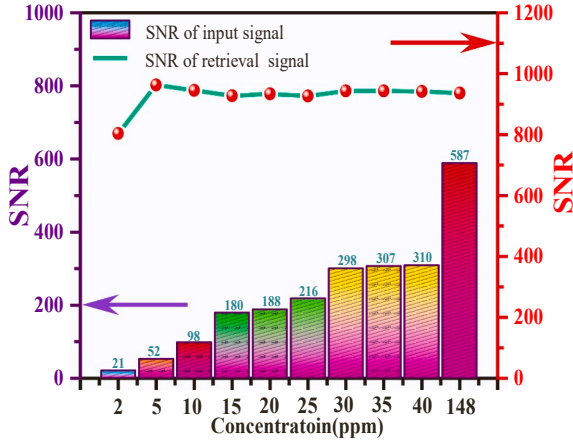
Fig. 6. SNR of PAS signals at different concentrations.
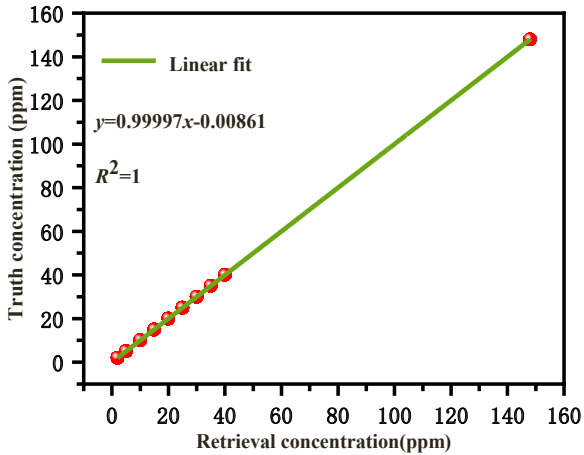

Fig. 7. Linear fit of truth and retrieval concentrations.

as depicted in Fig. 3.

Consequently, a comprehensive dataset which comprises 1.0*104 sets of methane PAS 2 *f* signals is assembled. Each signal is composed of 175 data points. In order to achieve consistency with the actual experimental signal and improve the generalization ability of the ResNets model, the comprehensive dataset is superposed with random noise (simulated by a random function) and optical interference noise (simulated by optical interference fringe formula) to form noisy methane PAS 2 *f* signals with noise mean value of 0.5685*10–3and noise variance of 7.5*10–3.All the pure methane PAS 2 *f* signal are regarded as the truth value or the model's labels.

Prior ResNets model training, the data sets are divided into a training set (90 %) and a test set (10 %), and all input signals are normalized to a range of [0,1] because the ResNets model is sensitive to data within this range.

During training, the hyperparameters are systematically adjusted within a narrow range to optimize the ResNets model's output signals. The gradient descent method is adopted to obtain the minimum loss function value and the optimal hyperparameters of the model. The Mean Square Error (MSE) is employed as the loss function in the model, as shown in formula (1).

$$\textbf{MSE} = \frac{\textbf{1}}{\textbf{\textit{m}}} \sum_{\textbf{\textit{i}}=\textbf{1}}^{\textbf{\textit{m}}=\textbf{350}} (\textbf{\textit{y}}(\textbf{\textit{i}}) - \widehat{\textbf{\textit{y}}}(\textbf{\textit{i}}))^{\textbf{2}} \tag{1}$$

Where i is the index corresponding to the whole output data or label of the input data, and m is the number of the data points of the truth label (m=350). $y(i)$ represents the 2 *f* signal output signal value of the model at the position i. $\widehat{y}(i)$ denotes the 2 *f* signal label value at the position i. In order to accelerate training speed and prevent gradient disappearance or explosion issues, two types of activation functions (ReLu and Sigmoid) are used in the model, as shown in expressions (2) and (3).

$$\textbf{ReLu} = \begin{cases} \textbf{\textit{x}} & \textbf{\textit{x}} > \textbf{0} \\ \textbf{0} \ \textit{otherwise} \end{cases} \tag{2}$$

$$\textbf{Sigmiod} = \frac{\textbf{1}}{\textbf{1} + \textbf{\textit{e}}^{-\textbf{\textit{x}}}} \tag{3}$$

The Adam optimizer ($\beta_1 = 0.9$ and $\beta_2 = 0.999$) is utilized to refine the ResNets model's performance. After rigorous hyperparameters validation, the whole model achieves optimal convergence at epochs of 6.0*103, a learning rate of 2*10–6, and a batch size of 1.6*103.

In order to evaluate the performance of the ResNets model in filtering noise, some residual plots between the truth signal and the retrieval signal of the ResNets model are analyzed, as illustrated in Fig. 5. The shapes of the output data coincide well with the truth signal without any noise perturbation.

Although the ResNets proposed in this paper emphasis on the whole 2 *f* signal, the number of data points of the two wings are more than that of the peak area, which are conducive to the learning of the model for the two wings. Therefore, the residuals in the wings are less than those of the peak areas, and the residuals of the two wings are almost zero.

In comparison to the standard deviation (SD) of the input signal's wings, the SD of the output signal's wings is nearly zero, and those results signify a significant reduction in noise. Those parameters summarized in Table 1. reveal that the SNR improvements range from 21 to 805 at 2 ppm, 52–962 at 5 ppm, and so forth up to 587–936 at 148 ppm, as shown in Fig. 6. Notably, the initial weak 2 ppm PAS 2 *f* signal has undergone a transformative enhancement by a factor of nearly 38, which achieves an SNR of 805.

In order to further improve the SNR of low-concentration signals for a better generalization ability, it is possible to increase the number of weak signals in the training set or the network depth to improve the model's learning ability for signals with low concentration (below 2 ppm). This strategy aims to bolster the model's proficiency in learning from weak signals, thereby also facilitating the extraction of information from high-concentration signals.

In order to evaluate the retrieval concentration effect of the ResNets model, the evaluation metrics employed include the retrieval accuracy (ACC = 1 − $|(\textbf{C} − \widehat{\textbf{C}})/\textbf{C}|$), absolute error (AE = $|(\textbf{C} − \widehat{\textbf{C}})|$), and determination coefficient (where C represents the truth concentration, C denotes the retrieval concentration from the ResNets model). These metrics are depicted in Fig. 6 and Fig. 7.

During the ResNets modeling process, the 2000 data sets are randomly chosen to form the test set. The Fig. 7 illustrates the retrieval results for the truth concentration against retrieval concentration from the ResNets model. The determination coefficient is $R2 = 1$, indicating a perfect fit.
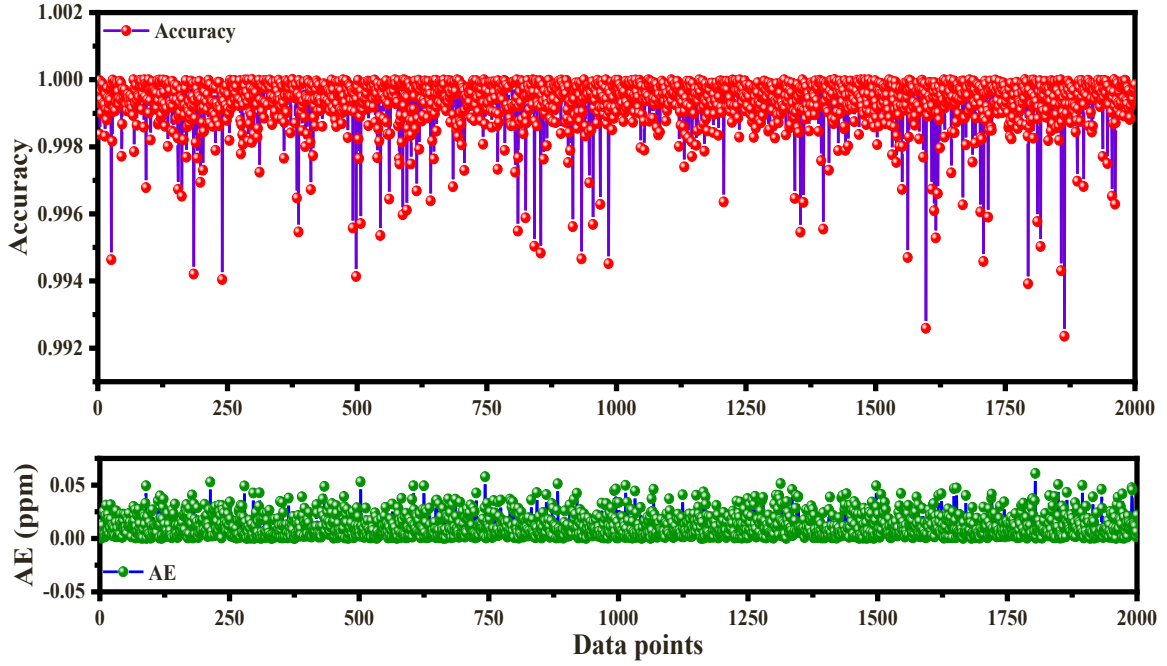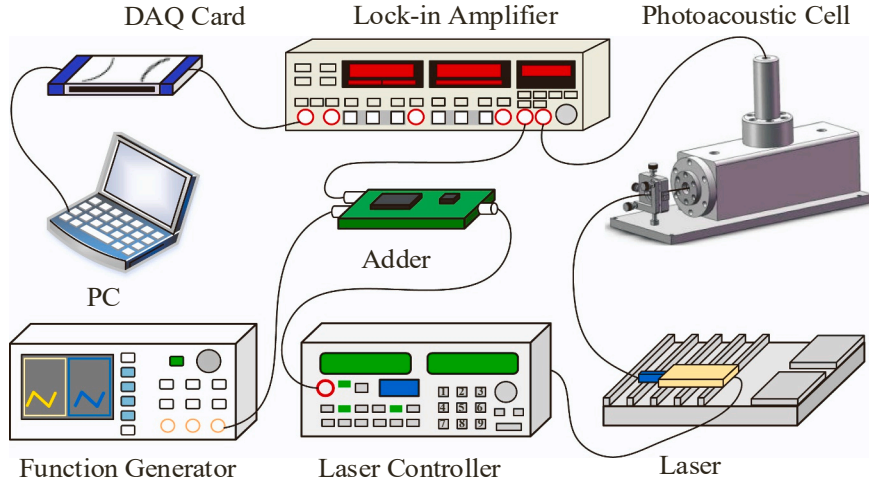
Fig. 8. ACC and AE for the ResNets model.

Fig. 9. Schematic diagram of the PAS experimental setup.

The [Fig. 8] illustrates the performance of the CH$_4$ PAS $2f$ signals in concentration regression prediction. The AE spans from 7.81 ppt to 0.061 ppm, demonstrating a narrow margin of error. The ACC results reveal that the ResNets exhibit superior linear correlation and high accuracy greater than 0.992. These findings substantiate that the ResNets model boasts a robust predictive capacity.

3. Experiments

3.1. Basic principle of PAS

The WMS theory is based on the Beer-Lambert Law, which describes the attenuation of a laser beam with intensity I_0 and frequency v_0 as the laser beam passes an absorbing gas medium. To produce the harmonic signals using a tunable diode laser, a sinusoidal modulation of angular frequency is superimposed upon the diode current. The individual harmonic components can be selected by using a lock-in amplifier set to detect at the n_{th} harmonic of the modulation frequency. The n_{th}

harmonic signal can be expressed as

$$A_n(v_0) = -\frac{1}{2^{n-1}} \frac{I_0(v_0)NLPS(T)}{n!} \frac{d^n\phi}{dv^n}\Big|_{v=v_0} \delta v^n \tag{4}$$

Where $I_0(v_0)$ is the incident intensity at frequency v_0, N is the concentration of the absorbing gas medium analyzed, L is the optical pathlength, P is the pressure, $S(T)$ is the temperature-dependent line intensity of the transition, ϕ is the normalized line-shape function of absorbing gas, δv is the frequency modulation amplitude.

When n is set to 2, the PAS $2f$ signal can be obtained. In this paper, the PAS $2f$ signal of the methane is selected to verify the feasibility of PAS sensor integrated with deep learning ResNets. This approach aims to leverage advanced computational techniques to enhance the sensitivity and accuracy of gas detection methods.
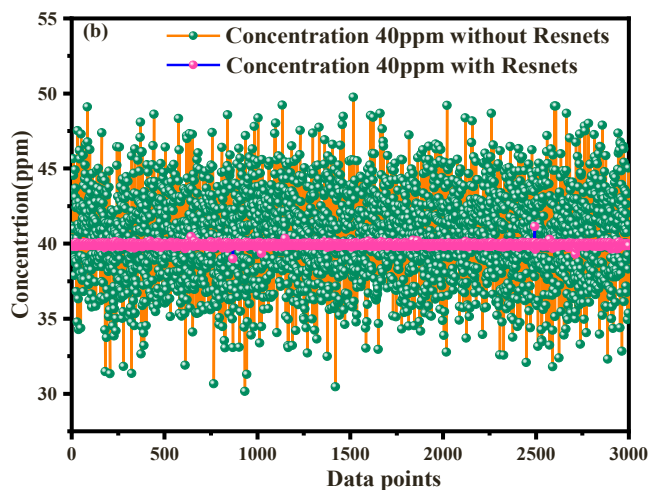
Fig. 10. (a)2 *f* signal with/without the ResNets for the measured data (b)Time-series of measurements at a constant concentration of 40 ppm using PAS system without (blackish green) and with (magenta) the ResNets.

3.2. Experimental configuration

In order to verify the generalization ability of the ResNets model on the actual experimental data sets, the PAS experimental configuration has been developed for simultaneous monitoring of critical greenhouse gas CH_4. The schematic of the PAS experimental setup is shown in . The fiber-coupled distributed feedback (DFB) diode laser operating at 1.653 μm was used for the detection of CH_4. A commercial diode laser controller (Stanford Research Systems LDC-501) was used for laser current and temperature controls. Laser wavelength scan was realized by feeding an external voltage ramp from a function generator (Siglent, SGD 1032X) to the laser diode current, which scanned the laser wavelengths back and forth across the absorption feature of each target molecule at a rate of 2 Hz, simultaneously.

Wavelength modulation and 2 *f* signal detection were employed in this work for sensitive trace gas detection. The wavelength modulation was achieved by adding a sine wave to the DFB laser diode current. The wavelength modulation was executed by superimposing a sine wave onto the DFB laser diode current. The voltage ramp and a 572 Hz sine waveform supplied by the lock-in amplifier (Healthy Photon, HPLIA) were combined with a home-made adder and then fed to the laser controller. The acoustic signal from the resonator was detected with the microphone (BSWA, MP201) and demodulated by the lock-in amplifier.

The PAS 2 *f* signals were subsequently digitized with a DAQ card (NI-USB-6353) and displayed on a laptop via a LabVIEW interface.

3.3. Results and discussion

Time-series measurements of 40 ppm CH_4 were performed to evaluate the measurement precision and stability of the PAS instrument. The measurement of CH_4 was performed by single detector signal with a scan rate of 2 Hz, namely, each data point was obtained in 0.5 s.
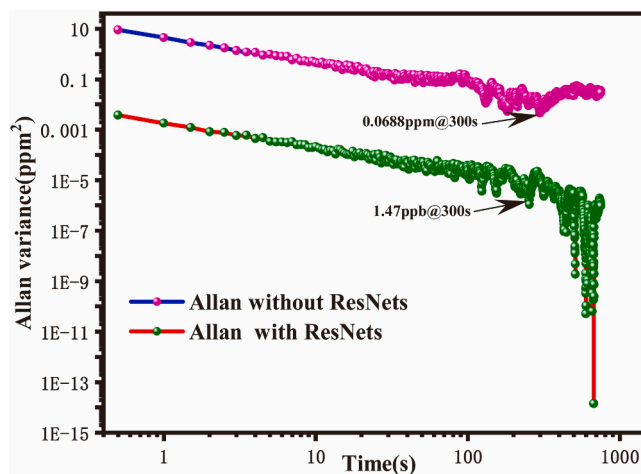

Fig. 12. Allan variance analysis on PAS system without ResNets (magenta) and with ResNets(blackish green).
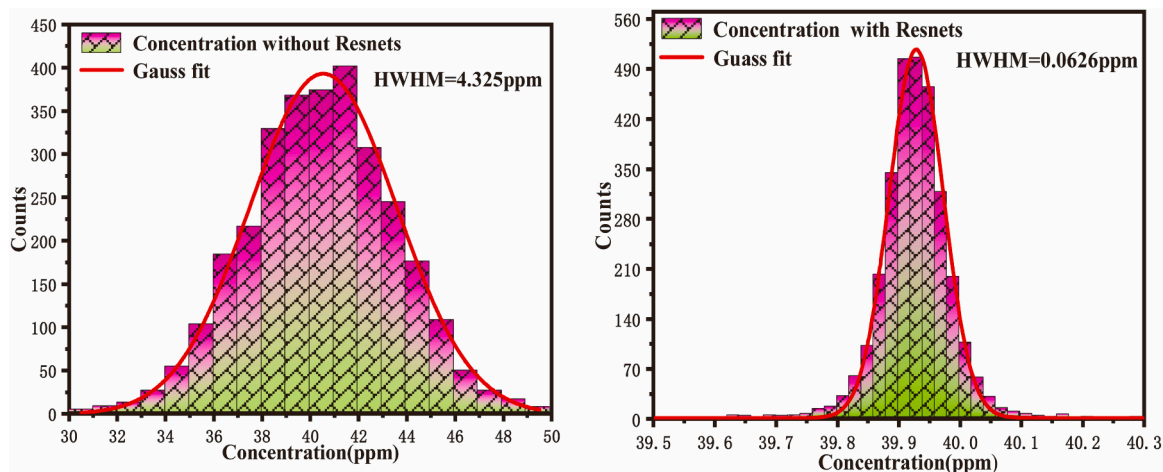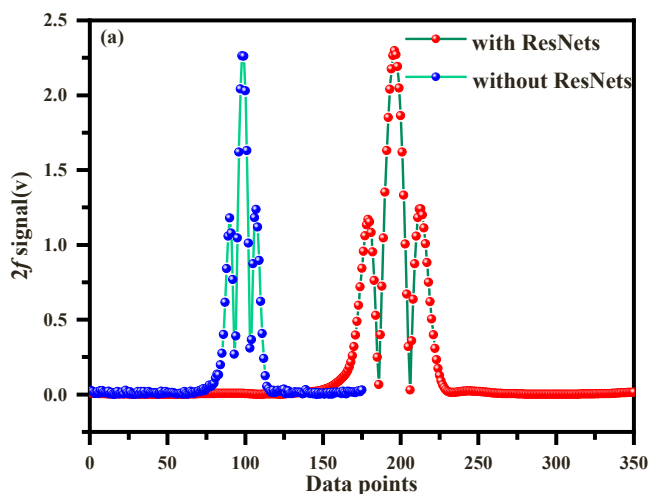

Fig. 11. Statistical histogram of CH_4 concentrations for about 1500 s without(left) and with ResNets(right).

The 3000 measurement data points were obtained during 1500 s continuous measurement. The experimental results are summarized in Fig. 10. The blackish-green line in the graph signifies the PAS system without ResNets, while the magenta line denotes the PAS system with ResNets.

From the difference value between the maximum and minimum retrieval concentrations, it can be found that the ResNets notably diminishes retrieval concentration fluctuations. The fluctuations are reduced from 19.59 ppm to 2.14 ppm. Additionally, the SD of the retrieval concentration is reduced from 3.02 ppm to 0.064 ppm.

For evaluation of the measurement precision of the PAS employing ResNets, histogram plot of measured data is shown in Fig. 11, which aids in evaluating the measurement precision. It can be seen that the data distribution exhibits a Gaussian profile, and the measurement precision quantified by the half width at half maximum (HWHM) is improved significantly from 4.325 ppm to 0.0626 ppm, which represents to an improvement by a factor of nearly 69.

For evaluation of the stability of the PAS employing ResNets, the Allan variance shown in Fig. 12 confirms the improvement introduced by ResNets. At the optimum integration time of approximately 300 s, the minimum detectable limit can be reduced from 0.0688 ppm to 1.47 ppb with ResNets, which leads to an improvement by a factor of nearly 46. The stability of the PAS system enhanced by ResNets is ascertained through Allan variance analysis. These results underscore the high sensitivity and precision, which demonstrates the superior performance of the PAS system developed with ResNets.

4. Conclusions

In conclusion, we have demonstrated that the ResNets can effectively suppress noise to further improve the minimum detectable limit, measurement precision and SNR of the PAS system. The PAS system employing ResNets not only improves the minimum detectable limit but also achieves a more than 46-fold improvement over traditional PAS systems, and the corresponding relative measurement precision is enhanced from 4.325 ppm to 0.0626 ppm, representing an improvement by a factor of nearly 69. When the concentration is 2 ppm, the SNR, which leverages ResNets, has been enhanced from 21 to 805 with a factor of nearly 38. As the concentration increases, the improvement efficiency gradually diminishes.

This promising result shows the high potential of this simple, cost-effective, compact PAS high-sensitivity gas sensor for various field applications.

CRediT authorship contribution statement

Jingjing Wang: Writing – review & editing, Funding acquisition, Conceptualization. **Junru Wang:** Conceptualization. **Shenlong Zha:** Funding acquisition, Conceptualization. **Yanan Cao:** Writing – original draft, Software, Project administration, Conceptualization. **Gang Cheng:** Project administration, Funding acquisition, Conceptualization. **Xing Tian:** Conceptualization. **Yan Li:** Data curation, Conceptualization. **Wenlei Fu:** Data curation, Conceptualization.

Declaration of Competing Interest

The authors declare no conflicts of interest.

Data Availability

Data will be made available on request.

Notes

The authors declare no conflicts of interest.

References

[1] V. Wittstock, L. Scholz, B. Bierer, A. Perez, J. Wöllenstein, S. Palzer, Design of a LED-based sensor for monitoring the lower explosion limit of methane, Sens. Actuator B-Chem. 247 (2017) 930.

[2] L. Shi, J. Wang, G. Zhang, X. Cheng, X. Zhao, A risk assessment method to quantitatively investigate the methane explosion in underground coal mine, Process. Saf. Environ. 107 (2017) 317.

[3] S. Iwaszenko, P. Kalisz, M. Słota, A. Rudzki, Detection of natural gas leakages using a laser-based methane sensor and UAV, Remote. Sens. 13 (2021) 510.

[4] J. Wang, X. Tian, Y. Dong, G. Zhu, J. Chen, T. Tan, K. Liu, W. Chen, X. Gao, Enhancing off-axis integrated cavity output spectroscopy (OA-ICOS) with radio frequency white noise for gas sensing, Opt. Express 27 (2019) 30517.

[5] J. Wang, X. Tian, Y. Dong, J. Chen, T. Tan, G. Zhu, W. Chen, X. Gao, High-sensitivity off-axis integrated cavity output spectroscopy implementing wavelength modulation and white noise perturbation, Opt. Lett. 44 (2019) 3298.

[6] Y. He, Y. Pan, G. Zhang, D. Ji, S. Tian, X. Xu, R. Zhang, Y. Wang, Tracking ammonia morning peak, sources and transport with 1 Hz measurements at a rural site in North China Plain, Atmos. Environ. 235 (2020) 117630.

[7] W. Chen, H. Yi, T. Wu, W. Zhao, C. Lengignon, G. Wang, E. Fertein, C. Coeur, Encyclopedia of Analytical Chemistry (2017).

[8] W. Chen, A.A. KOSTEREV, F.K. Tittel, X. Gao, W. Zhao, H2S trace concentration measurements using off-axis integrated cavity output spectroscopy in the near-infrared, Appl. Phys. B 90 (2008) 311.

[9] W. Zhao, X. Gao, W. Chen, W. Zhang, T. Huang, T. Wu, H. Cha, Wavelength modulated off-axis integrated cavity output spectroscopy in the near infrared, Appl. Phys. B 86 (2007) 353.

[10] G.S. Engel, W.S. Drisdell, F.N. Keutsch, E.J. Moyer, J.G. Anderson, Ultrasensitive near-infrared integrated cavity output spectroscopy technique for detection of CO at 1.57 μm: new sensitivity limits for absorption measurements in passive optical cavities, Appl. Opt. 45 (2006) 9221.

[11] E. Richard, B. Giel, P. Rudy, M. Gerard, Cavity enhanced absorption and cavity enhanced magnetic rotation spectroscopy, Rev. Sci. Instrum. 69 (1998) 3763.

[12] V.L. Kasyutich, P.A. Martin, R.J. Holdsworth, An off-axis cavity-enhanced absorption spectrometer at 1605 nm for the $^{12}CO_2$/$^{13}CO_2$ measurement, Appl. Phys. B 85 (2006) 413.

[13] B.C. Smith, Fundamentals of Fourier Transform Infrared Spectroscopy, CRC Press, 2011.

[14] L. Zhang, M. Zhang, T. Chen, D. Liu, S. Hong, D. Dai, Ultrahigh-resolution on-chip spectrometer with silicon photonic resonators, Opto-Electron. Adv. 5 (2022) 210100.

[15] R. Cui, L. Dong, H. Wu, W. Ma, L. Xiao, S. Jia, W. Chen, F.K. Tittel, Three-dimensional printed miniature fiber-coupled multipass cells with dense spot

patterns for ppb-level methane detection using a near-IR diode laser, Anal. Chem. 92 (2020) 13034.

[16] T. Wei, H. Wu, L. Dong, R. Cui, S. Jia, Palm-sized methane TDLAS sensor based on a mini-multi-pass cell and a quartz tuning fork as a thermal detector, Opt. Express 2021 29 (2021) 12357.

[17] T. Liang, S. Qiao, Y. Chen, Y. He, Y. Ma, High-sensitivity methane detection based on QEPAS and H-QEPAS technologies combined with a self-designed 8.7 kHz quartz tuning fork, Photoacoustics 36 (2024) 100592.

[18] B. Li, G. Menduni, M. Giglio, P. Patimisco, A. Sampaolo, A. Zifarelli, H. Wu, T. Wei, V. Spagnolo, L. Dong, Quartz-enhanced photoacoustic spectroscopy (QEPAS) and Beat frequency-QEPAS techniques for air pollutants detection: a comparison in terms of sensitivity and acquisition time, Photoacoustics 31 (2023) 100479.

[19] Y. Ma, R. Lewicki, M. Razeghi, F.K. Tittel, QEPAS based ppb-level detection of CO and N_2O using a high-power CW DFB-QCL, Opt. Express 21 (2013) 1008.

[20] G. Menduni, A. Zifarelli, A. Sampaolo, P. Patimisco, M. Giglio, N. Amoroso, H. Wu, L. Dong, R. Bellotti, V. Spagnolo, High-concentration methane and ethane QEPAS detection employing partial least squares regression to filter out energy relaxation dependence on gas matrix composition, Photoacoustics 26 (2022) 100349.

[21] S. Li, J. Lu, Z. Shang, X. Zeng, S. Yuan, H. Wu, Y. Pan, A. Sampaolo, P. Patimisco, V. Spagnolo, L. Dong, Compact quartz-enhanced photoacoustic sensor for ppb-level ambient NO_2 detection by use of a high-power laser diode and a grooved tuning fork, Photoacoustics 25 (2022) 100325.

[22] X. Yin, L. Dong, H. Wu, M. Gao, L. Zhang, X. Zhang, L. Liu, X. Shao, F.K. Tittel, Compact QEPAS humidity sensor in SF_6 buffer gas for high-voltage gas power systems, Photoacoustics 25 (2022) 100319.

[23] W. Chen, S. Qiao, Y. He, J. Zhu, K. Wang, L. Xiao, Y. Ma, Quasi-distributed quartz enhanced photoacoustic spectroscopy sensing based on hollow waveguide micropores, Opt. Lett. 49 (2024) 2765.

[24] Y. Liu, S. Qiao, C. Fang, Y. He, H. Sun, J. Liu, Y. Ma, A highly sensitive LITES sensor based on a multi-pass cell with dense spot pattern and a novel quartz tuning fork with low frequency, Opto-Electron. Adv. 7 (2024) 230230.

[25] H. Sun, S. Qiao, Y. He, Y. Liu, Y. Ma, Highly sensitive CH_4, C_2H_2 and CO simultaneous measurement LITES sensor based on multi-pass cell with overlapped spots pattern and QTFs with low resonant frequency, Opt. Express 32 (2024) 28183.

[26] H. Sun, Y. He, S. Qiao, Y. Liu, Y. Ma, Highly sensitive and real-simultaneous CH_4/C_2H_2 dual-gas LITES sensor based on Lissajous pattern multi-pass cell, Opto-Electron, Sci 3 (2024) 240013.

[27] M.A. Abbas, Q. Pan, J. Mandon, S.M. Cristescu, F.J.M. Harren, A. Khodabakhsh, Time-resolved midinfrared dual-comb spectroscopy, Sci. Rep. -UK 9 (2019) 17247.

[28] Q. Wang, Z. Wang, H. Zhang, S. Jiang, Y. Wang, W. Jin, W. Ren, Dual-comb photothermal spectroscopy, Nat. Commun. 13 (2022) 1.

[29] Z. Wang, Q. Nie, H. Sun, Q. Wang, S. Borri, P.D. Natale, W. Ren, Cavity-enhanced photoacoustic dual-comb spectroscopy, Light-Sci. Appl. 13 (2024) 2047.

[30] B. Xu, X. Fan, S. Wang, Z. He, Sub-femtometer-resolution absolute spectroscopy with sweeping electro-optic combs, Opto-Electron. Adv. 5 (2022) 210023.

[31] S.D. Wankel, Y. Huang, M. Gupta, R. Provencal, P.R. Girguis, Characterizing the distribution of methane sources and cycling in the deep sea via in situ stable isotope analysis, 2013, Environ. Sci. Technol. 47 (2013) 1478.

[32] M. Mazurenka, A.J. Orr-Ewing, R. Peverall, G.A.D. Ritchie, Cavity ring-down and cavity enhanced spectroscopy using diode lasers, Annu. Rep. Prog. Chem., Sect. C. 101 (2005) 100.

[33] J. Dang, L. Kong, C. Zheng, Y. Wang, Y. Su, H. Yu, An open-path sensor for simultaneous atmospheric pressure detection of CO and CH_4 around 2.33 μm, Opt. Lasers Eng. 123 (2019) 1.

[34] H. Yang, X. Bu, Y. Cao, Y. Song, A methane telemetry sensor based on near-infrared laser absorption spectroscopy, Infrared Phys. Technol. 114 (2021) 103670.

[35] S. Qiao, Y. He, H. Sun, P. Patimisco, A. Sampaolo, V. Spagnolo, Y. Ma, Ultra-highly sensitive dual gases detection based on photoacoustic spectroscopy by exploiting a long-wave, high-power, wide-tunable, single-longitudinal-mode solid-state laser, Sci. Appl. 13 (2024) 100.

[36] C. Zhang, Y. He, S. Qiao, Y. Liu, Y. Ma, High-sensitivity trace gas detection based on differential Helmholtz photoacoustic cell with dense spot pattern, Photoacoustics 38 (2024) 100634.

[37] Y. Cao, Y. Ma, X. Cheng, G. Cheng, X. Tian, S. Zha, H. Ma, J. Wang, Z. Xu, Parameter-tuning stochastic resonance as a tool to enhance wavelength modulation spectroscopy using a dense overlapped spot pattern multi-pass cell, Opt. Express 30 (2022) 32010.

[38] G. Liu, B. Fan, Infrared gas detection technology based on parameter-tuning stochastic resonance, Opt. Eng. 58 (2019) 015107.

[39] B. Fan, Y. Zhang, Y. He, K. You, M. Li, D. Yu, H. Xie, B. Lei, Adaptive monostable stochastic resonance for processing UV absorption spectrum of nitric oxide, Opt. Express 28 (2020) 9811.

[40] R. Luo, J. Popp, T. Bocklitz, Deep learning for raman spectroscopy: a review, Analytica 3 (2022) 287.

[41] K. Ghosh, A. Stuke, Milica Todorović, Peter Bjørn Jørgensen, Mikkel N. Schmidt, Aki Vehtari, P. Rinke, Deep learning spectroscopy: neural networks for molecular excitation spectra, Adv. Sci. 6 (2019) 1801367.

Yanan Cao is an Associate Professor at Anhui University of Technology. He received Ph.D. degree in optics from the University of Science and Technology of China in 2018. His current research interests include optical design and simulation and laser spectroscopy.

Wenlei Fu is a postgraduate student in Anhui University of Science and Technology, China. Her research focuses mainly on high sensitivity optical fiber acoustic detection technology.

Yan Li is a postgraduate student in Anhui University of Science and Technology, China. Her research focuses mainly on optical sensor and deep learning algorithms.

Gang Cheng is an Associate Professor at Anhui University of Technology. He received his Ph.D. degree from the University of Science and Technology of China in 2019. His research interests are absorption spectroscopy and photoacoustic spectroscopy for trace gases.

Xing Tian is a lecturer at Anhui University of Technology. He received his Ph.D. degree from the University of Science and Technology of China in 2019. His research interest is trace gas detection using laser absorption spectroscopic techniques.

Jingjing Wang received the Ph.D. degree in Hefei Institute of Physical Science, Chinese Academy of Sciences from the University of Science and Technology, China in 2021. From 2022 to the present, she has worked as a postdoctoral researcher in the Department of Atmospheric and Oceanic Sciences, Fudan University, Shanghai, China. Her research interests include ground-based remote sensing of CH_4 and CO_2 and sensing equipment.

Shenlong Zha is an Associate Professor at Anqing Normal University. He received Ph.D. degree in optics from the University of Science and Technology of China in 2017. His current research interests include optical design and photoacoustic spectroscopy.
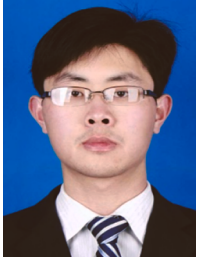
Junru Wang is a research associate in College of Electronic Engineering, at National University of Defense and Technology, China. He got Ph. D. degree in 2021 from University of Science and Technology of China. His research mainly focuses on optical protective materials and low-temperature plasma technology.